

Taming Stable Diffusion for Computed Tomography Blind Super-Resolution

Chunlei Li^{1*}, Yilei Shi^{1*}, Haoxi Hu², Jingliang Hu¹, Xiao Xiang Zhu³, and Lichao Mou^{1(✉)}

¹ MedAI Technology (Wuxi) Co. Ltd., Wuxi, China
 lichao.mou@medimagingai.com

² Northeastern University, Boston, USA
³ Technical University of Munich, Munich, Germany

Abstract. High-resolution computed tomography (CT) imaging is essential for medical diagnosis but requires increased radiation exposure, creating a critical trade-off between image quality and patient safety. While deep learning methods have shown promise in CT super-resolution, they face challenges with complex degradations and limited medical training data. Meanwhile, large-scale pre-trained diffusion models, particularly Stable Diffusion, have demonstrated remarkable capabilities in synthesizing fine details across various vision tasks. Motivated by this, we propose a novel framework that adapts Stable Diffusion for CT blind super-resolution. We employ a practical degradation model to synthesize realistic low-quality images and leverage a pre-trained vision-language model to generate corresponding descriptions. Subsequently, we perform super-resolution using Stable Diffusion with a specialized controlling strategy, conditioned on both low-resolution inputs and the generated text descriptions. Extensive experiments show that our method outperforms existing approaches, demonstrating its potential for achieving high-quality CT imaging at reduced radiation doses. Our code will be made publicly available.

Keywords: CT super-resolution · Stable Diffusion · fine-tuning.

1 Introduction

Computed tomography (CT) is an indispensable imaging modality in modern healthcare, serving a crucial role in disease diagnosis, treatment planning, and clinical research [1]. The diagnostic value of CT images heavily depends on their spatial resolution, driving the continuous pursuit of high-resolution CT imaging techniques [2]. However, achieving high-resolution CT scans often requires increased radiation exposure, which poses potential health risks to patients [3]. This fundamental trade-off between image quality and radiation dose has motivated extensive research in CT super-resolution methods, aiming to generate high-resolution CT images from low-dose acquisitions [4].

* Equal contribution.

Recent years have witnessed remarkable progress in image super-resolution, primarily driven by deep learning approaches. Early efforts [5,8,7] typically rely on simulated training data with simplified, uniform degradation models, such as bicubic downsampling. Although these methods show promise in controlled settings, they often underperform when applied to real-world low-resolution images characterized by complex, unknown degradations. To address these limitations, blind image super-resolution methods [12,10,11,31] have gained increasing attention, particularly in medical imaging applications where degradation patterns can be highly variable and unpredictable. Recent work has demonstrated success in radiographs and MRI through blind super-resolution approaches that generalize across degradation types [22,23].

Despite these remarkable advances, the performance of learning-based super-resolution methods is inherently tied to the availability of high-quality training data. Unlike natural image domains with abundant data, medical imaging faces data scarcity due to privacy concerns and regulatory requirements, creating a barrier to developing robust super-resolution models.

Recently, large-scale pre-trained text-to-image diffusion models, particularly Stable Diffusion [17], have demonstrated astonishing capabilities in generating highly detailed images. Trained on vast collections of image-text pairs, these models have not only revolutionized image generation but have also shown promise results when adapted to various vision tasks, including image segmentation and enhancement [24,25,26,27]. This success motivates our investigation into leveraging Stable Diffusion for CT super-resolution, utilizing its rich prior knowledge of image structure and detail synthesis.

However, applying Stable Diffusion to CT super-resolution presents challenges. A fundamental obstacle is the domain gap between the model’s training data—comprising internet-scale natural image-text pairs—and CT images. Direct application of Stable Diffusion risks synthesizing features characteristic of natural images, which is problematic given CT images’ distinct properties in grayscale distributions, structural patterns, and texture characteristics.

To address this issue, we propose a novel framework that adapts Stable Diffusion for CT blind super-resolution. First, we employ a practical degradation model [12] to synthesize realistic low-quality images. Second, we utilize LLaVA-Med [21], a specialized medical vision-language model, to generate anatomical descriptions from these degraded images, which serve as semantic prompts for the subsequent super-resolution process. Third, we adapt Stable Diffusion by freezing its pre-trained layers and introducing a side-controlling strategy to generate high-resolution CT images conditioned on low-resolution inputs and text prompts. Our approach effectively bridges the gap between Stable Diffusion’s general-purpose generative capabilities and specialized medical imaging requirements. Our main contributions are:

- We present the first attempt to adapt Stable Diffusion for medical image super-resolution.

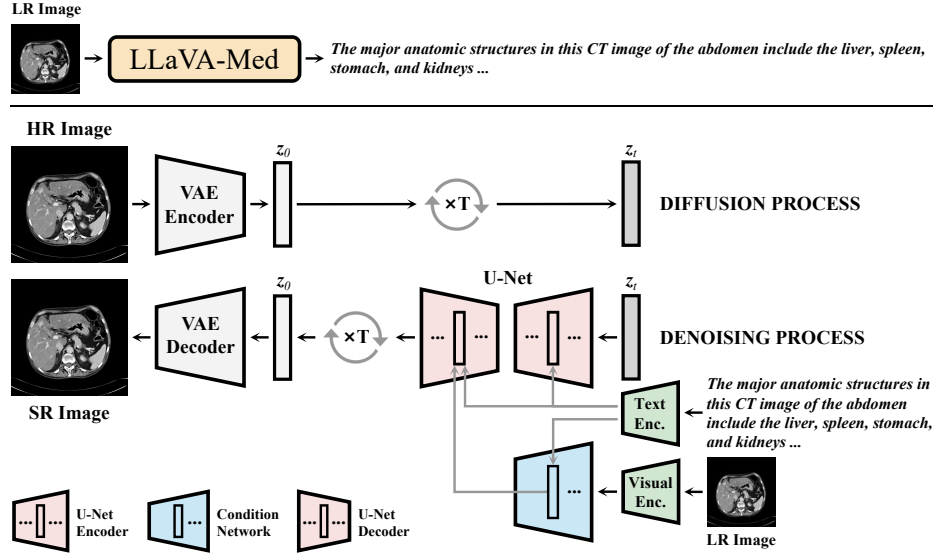


Fig. 1. Overview of our proposed framework. The pipeline consists of two stages: (1) text description generation from low-resolution images using LLaVA-Med, and (2) image super-resolution through the proposed side-controlling strategy, which integrates both the generated text prompts and low-resolution images into the Stable Diffusion model.

- We propose a two-stage framework combining LLaVA-Med with Stable Diffusion, enabling text-guided super-resolution for medical imaging, along with a side-controlling approach to address domain shift.
- State-of-the-art performance on CT super-resolution tasks, surpassing existing methods.

2 Method

As shown in Fig. 1, our framework consists of two main stages: text prompt generation and taming Stable Diffusion for super-resolution through the side-controlling strategy. The key innovation lies in fusing visual constraints from low-resolution inputs with semantic guidance derived from text prompts, enabling precise control over the pre-trained Stable Diffusion model.

2.1 Text Prompt Generation

To make full use of the generative potential of Stable Diffusion for super-resolution, we employ LLaVA-Med [21] to generate descriptive text prompts from low-dose CT images.

Given a low-resolution image \mathbf{x}_{lr} and an instruction \mathbf{s} (e.g., *Describe main anatomical structures present in the image*) as inputs, LLaVA-Med produces a corresponding textual description \mathbf{p} , formulated as:

$$\mathbf{p} = \mathcal{F}_{\text{LLaVA-Med}}(\mathbf{x}_{lr}, \mathbf{s}). \quad (1)$$

The resulting \mathbf{p} provides valuable semantic information, particularly anatomical structures, which is crucial for medical imaging tasks. This description is then fed into Stable Diffusion as a text prompt, along with \mathbf{x}_{lr} .

2.2 Side-Controlling

To bridge the domain gap between natural and medical images while leveraging the strength of Stable Diffusion, we propose a side-controlling strategy. This approach synergizes text prompts (see Section 2.1) and low-resolution images to provide complementary guidance during generation. The textual prompts offer high-level contextual understanding, while the low-resolution images introduce spatial and structural constraints. These constraints are injected into the Stable Diffusion model in a side-controlling manner. By jointly utilizing these two types of control signals, our approach ensures that the generation of high-resolution images considers both semantic context and fine-grained textures required in medical imaging.

Our strategy comprises three key components: a text encoder for prompt encoding, a visual encoder that encodes low-resolution images, and a condition network that incorporates the encoded features into the diffusion model to guide the generation process.

Text Encoder We leverage the text encoder of CLIP [28] to extract linguistic features, as it is pre-trained on massive image-text pairs. We freeze the text encoder to preserve its robust generalization in image-text alignment. Let \mathcal{E}_T denote the text encoder, the encoding process can be written as:

$$\mathbf{f}_p = \mathcal{E}_T(\mathbf{p}). \quad (2)$$

Visual Encoder The visual encoder extracts visual features from low-resolution inputs to guide the generative process. We utilize the pre-trained VAE encoder of Stable Diffusion, denoted as \mathcal{E}_V , to project \mathbf{x}_{lr} into the VAE’s latent space:

$$\mathbf{f}_{lr} = \mathcal{E}_V(\mathbf{x}_{lr}). \quad (3)$$

Condition Network The latent representation of a high-resolution image is obtained by the pre-trained VAE encoder, denoted \mathbf{z}_0 . Both diffusion and de-noising processes occur in the latent space. During diffusion, Gaussian noise with variance $\beta_t \in (0, 1)$ at time t is added to \mathbf{z}_0 to produce the noisy latent:

$$\mathbf{z}_t = \sqrt{\bar{\alpha}_t} \mathbf{z}_0 + \sqrt{1 - \bar{\alpha}_t} \epsilon, \quad (4)$$

where $\epsilon \sim \mathcal{N}(0, \mathbf{I})$, $\alpha_t = 1 - \beta_t$, and $\bar{\alpha}_t = \prod_{s=1}^t \alpha_s$. At sufficiently large t , the latent \mathbf{z}_t approximates a standard Gaussian distribution.

We define the entire U-Net in the Stable Diffusion model as $\mathcal{F}_{\text{U-Net}}$. In the denoising process, we clone a trainable copy of the U-Net encoder \mathcal{E}_{U} as our condition network (denoted as $\mathcal{F}_{\text{COND}}$), which processes condition information and outputs control signals. This copy strategy provides a good weight initialization for the condition network. Then, the concatenation of the condition \mathbf{f}_{lr} and the noisy latent \mathbf{z}_t at time t forms \mathbf{z}'_t . This concatenated representation, along with the textual embedding \mathbf{f}_p , are fed into $\mathcal{F}_{\text{COND}}$. At each block of $\mathcal{F}_{\text{COND}}$, the output is skip-connected to the corresponding block of the U-Net decoder \mathcal{D}_{U} in Stable Diffusion, facilitating the effective integration of the conditional signals.

Meanwhile, \mathbf{f}_p and \mathbf{z}_t are fed into $\mathcal{F}_{\text{U-Net}}$. We denote the output of the i -th block of \mathcal{D}_{U} as \mathbf{o}_i . In the i -th block where control information is involved, the calculation proceeds as follows:

$$\mathbf{o}_i = \mathcal{D}_{\text{U}}^i(\mathbf{o}_{i-1}, \mathbf{f}_p) + \mathcal{F}_{\text{COND}}^i(\mathbf{z}'_t, \mathbf{f}_p). \quad (5)$$

The final high-resolution image is generated by mapping the denoised latent \mathbf{z}'_0 through the VAE decoder \mathcal{D}_{V} :

$$\mathbf{x}'_{hr} = \mathcal{D}_{\text{V}}(\mathbf{z}'_0). \quad (6)$$

2.3 Training Objective

We train a noise prediction model ϵ_θ conditioned on low-resolution images and text prompts:

$$\mathcal{L} = \mathbb{E}_{\mathbf{z}_0, \mathbf{f}_{lr}, t, \mathbf{f}_p, \epsilon \sim \mathcal{N}} \left[\left\| \epsilon - \epsilon_\theta(\mathbf{z}_t, t, \mathbf{f}_{lr}, \mathbf{f}_p) \right\|_2^2 \right]. \quad (7)$$

3 Experiments

3.1 Datasets and Evaluation Metrics

We evaluate our method on two widely used public CT image datasets: Pancreas [18] and 3D-IRCADb [18]. The Pancreas dataset contains 19,328 CT slices with a resolution of 512×512 pixels from 82 patients. For our experiments, we utilize 5,638 slices from 65 patients for training and 1,421 slices from 17 patients for testing. The 3D-IRCADb dataset comprises 2,823 CT slices (512×512 resolution) from 20 patients, with 1,663 slices from 16 patients for training and 411 slices from 4 patients for testing. Following [29], we standardize the data by clipping Hounsfield unit values to $[-135, 215]$ and simulate low-dose noise by setting the blank flux to 0.5×10^5 . We adopt the degradation pipeline from Real-ESRGAN [12] to generate low-resolution images at 256×256 and 128×128 pixels, corresponding to upscaling factors of $\times 2$ and $\times 4$, respectively.

For evaluation, we employ two metrics: peak signal-to-noise ratio (PSNR) and structural similarity index measure (SSIM) [20]. They are widely accepted reference-based fidelity measures for assessing image quality.

Table 1. Quantitative comparison with state-of-the-art methods on two public datasets at scale factors of $\times 2$ and $\times 4$. Results in **bold** and underlined indicate the best and second-best performance, respectively.

	Pancreas				3D-IRCADb			
	$\times 2$		$\times 4$		$\times 2$		$\times 4$	
	PSNR	SSIM	PSNR	SSIM	PSNR	SSIM	PSNR	SSIM
SRGAN	26.8732	0.7701	25.6810	0.7539	25.5262	0.7425	24.5693	0.7206
EDSR	28.8972	0.8364	27.8862	0.8105	28.2912	0.7973	27.1478	0.7882
ESRGAN	27.9114	0.8073	26.7801	0.7818	26.6362	0.7492	25.1963	0.7366
RCAN	29.1973	0.8442	28.0183	0.8236	28.5914	0.7969	27.2284	0.7891
IKC	29.7129	0.8709	28.4862	0.8449	29.4764	0.8254	28.2687	0.7914
DAN	30.0293	0.8813	28.5829	0.8589	29.5708	0.8269	28.3362	0.7993
RealSR	28.8903	0.8256	27.2931	0.8023	28.7308	0.8081	26.8275	0.7692
Real-ESRGAN	28.7841	0.8179	26.9721	0.7993	27.0132	0.7707	25.4315	0.7419
SwinIR	28.9764	0.8378	27.7532	0.8043	28.6215	0.8012	27.1922	0.7891
SR3	25.6895	0.7525	24.8917	0.7315	25.2515	0.7402	23.9709	0.7059
DFD-DCC	28.7357	0.8104	27.8532	0.8073	26.6801	0.7821	25.4221	0.7137
MDA-SR	28.7601	0.8647	27.0821	0.8290	27.7921	0.8082	26.8732	0.7671
RGT	28.9527	0.8755	27.8601	0.8575	29.5512	0.8253	28.3097	0.7899
Ours	32.0349	0.8933	30.8082	0.8748	30.8707	0.8370	29.6483	0.8113

3.2 Implementation Details

All experiments are conducted using PyTorch on NVIDIA RTX 4090Ti GPUs. We train the model for 150K iterations using the Adam optimizer [19] with a learning rate of 5×10^{-5} and a batch size of 2 per GPU across 8 GPUs. During inference, we employ spaced DDPM sampling [30] with 50 timesteps.

3.3 Comparison with State-of-the-Art Methods

We compare our method against twelve state-of-the-art approaches: SRGAN [5], EDSR [7], ESRGAN [6], RCAN [8], IKC [10], DAN [11], RealSR [31], Real-ESRGAN [12], SwinIR [9], SR3 [13], DFD-DCC [14], MDA-SR [15], and RGT [16]. Table 1 demonstrates our framework’s superior performance across both datasets and scaling factors. On the Pancreas dataset, our method surpasses the second-best approach by 2.0056dB/0.012 and 2.2253dB/0.0159 in PSNR and SSIM for $\times 2$ and $\times 4$ scaling factors, respectively. Similarly, for the 3D-IRCADb dataset, we achieve improvements of 1.2999dB/0.0101 and 1.3121dB/0.012 in PSNR and SSIM across both scales compared to the next best method.

Fig. 2 presents a qualitative comparison between our method and competing approaches. Our results demonstrate superior artifact suppression, particularly in edge regions and internal structures, while other methods suffer from artifacts and blurred structures. Furthermore, our approach produces semantically accurate and detail-rich reconstructions, preserving clear edges, fine details, and textural structures.

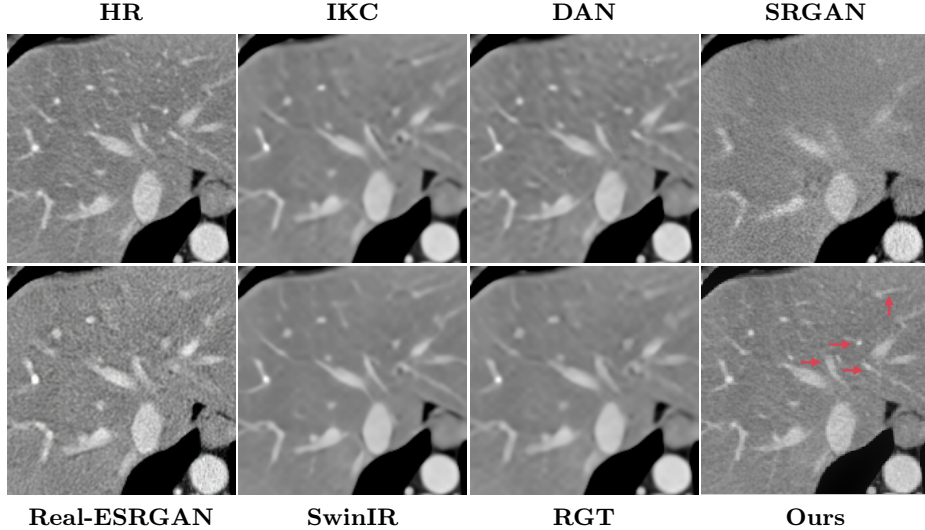


Fig. 2. Qualitative results on the 3D-IRCADb dataset with a scale factor of 4. The top-left image shows a zoomed-in region of a high-resolution image, focusing on the liver and its internal structures for better visualization. Subsequent images display super-resolution results from various methods. The bottom-right image presents our proposed method’s output, with red arrows highlighting regions where our approach generates more accurate and detailed structures.

3.4 Ablation Studies

We conduct comprehensive ablation studies to validate each component of our framework.

Text Prompting Analysis We evaluate the impact of text-based guidance by comparing our full model against variants with omitted text prompts or modified LLaVA-Med instructions. Results in Table 2 show that removing text prompts significantly degrades performance, highlighting their crucial role in providing valuable prior knowledge. Notably, our framework demonstrates robustness to minor variations in LLaVA-Med instructions, maintaining consistent performance—a crucial feature for practical applications.

Visual Encoder We examine two configurations of the pre-trained VAE encoder from Stable Diffusion: learnable versus frozen. Results in Fig. 3 indicate superior performance with the learnable configuration, likely due to its ability to adapt to medical image-specific features.

Condition Network We investigate two initialization strategies for the condition network: pre-trained weights from Stable Diffusion’s UNet versus random

Table 2. Ablation study on the Pancreas dataset comparing different instructions to LLaVA-Med. \times : no text prompts; \spadesuit : using instruction *Describe the anatomical structures in this CT image of the abdomen*; \diamond : using instruction *List the major anatomic structures in this CT image of the abdomen*.

Instruction	$\times 2$		$\times 4$	
	PSNR	SSIM	PSNR	SSIM
\times	29.9012	0.8728	28.3015	0.8505
\spadesuit	32.0163	0.8928	30.7891	0.8724
\diamond	32.0349	0.8933	30.8082	0.8748

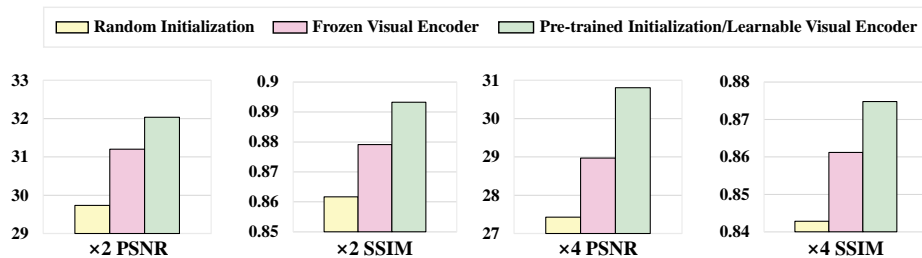


Fig. 3. Ablation study results on the Pancreas dataset. We evaluate the following configurations: random initialization (yellow) vs. pre-trained initialization (green), and frozen visual encoder (pink) vs. learnable visual encoder (green), for both $\times 2$ and $\times 4$ upscaling factors. Performance is measured using PSNR and SSIM. Our method consistently achieves the best results across all experimental settings.

initialization. Fig. 3 shows that pre-trained initialization yields better results in both PSNR and SSIM. This suggests that leveraging pre-trained weights enables more effective integration of conditional signals from low-resolution medical images and text prompts, ultimately leading to improved high-resolution image generation.

4 Conclusion

In this work, we present a novel framework for CT blind super-resolution that successfully adapts Stable Diffusion to the medical imaging domain. By using LLaVA-Med for semantic description generation and introducing a side-controlling strategy, we effectively bridge the domain gap between natural and medical images. Our experimental results validate the framework’s effectiveness, showing consistent improvements over existing methods.

The success of our approach suggests that pre-trained generative models can be effectively adapted for specialized medical imaging tasks. Looking ahead, the framework could be extended to other imaging modalities, and the integration of more sophisticated anatomical priors could further improve performance. We believe our work represents a step toward achieving high-quality CT imaging

at reduced radiation doses, with potential impact on patient care through safer diagnostic procedures.

Future work could explore extending this framework to other medical imaging modalities such as MRI and ultrasound to further validate its generalizability in various healthcare applications.

References

1. Chu, Y., Zhou, L., Luo, G., Qiu, Z., Gao, X.: Topology-preserving computed tomography super-resolution based on dual-stream diffusion model. In: Medical Image Computing and Computer Assisted Intervention, pp. 260–270. (2023)
2. Akagi, M., Nakamura, Y., Higaki, T., Narita, K., Honda, Y., Zhou, J., Yu, Z., Akino, N., Awai, K.: Deep learning reconstruction improves image quality of abdominal ultra-high-resolution CT. *European Radiology* **29**, 6163–6171 (2019)
3. You, C., Cong, W., Vannier, M.W., Saha, P.K., Hoffman, E.A., Wang, G., Li, G., Zhang, Y., Zhang, X., Shan, H., Li, M., Ju, S., Zhao, Z., Zhang, Z.: CT super-resolution GAN constrained by the identical, residual, and cycle learning ensemble (GAN-CIRCLE). *IEEE Transactions on Medical Imaging* **39**(1), 188–203 (2019)
4. Chen, Y., Zheng, Q., Chen, J.: Double paths network with residual information distillation for improving lung CT image super resolution. *Biomedical Signal Processing and Control* **73**, 103412 (2022)
5. Ledig, C., Theis, L., Huszar, F., Caballero, J., Cunningham, A., Acosta, A., Aitken, A. P., Tejani, A., Totz, J., Wang, Z., Shi, W.: Photo-realistic single image super-resolution using a generative adversarial network. In: IEEE Conference on Computer Vision and Pattern Recognition, pp. 4681–4690. (2017)
6. Wang, X., Yu, K., Wu, S., Gu, J., Liu, Y., Dong, C., Qiao, Y., Loy, C.C.: ESRGAN: Enhanced super-resolution generative adversarial networks. In: European Conference on Computer Vision Workshops, pp. 63–79. (2018)
7. Lim, B., Son, S., Kim, H., Nah, S., Mu Lee, K.: Enhanced deep residual networks for single image super-resolution. In: IEEE Conference on Computer Vision and Pattern Recognition Workshops, pp. 136–144. (2017)
8. Zhang, Y., Li, K., Li, K., Wang, L., Zhong, B., Fu, Y.: Image super-resolution using very deep residual channel attention networks. In: European Conference on Computer Vision, pp. 286–301. (2018)
9. Liang, J., Cao, J., Sun, G., Zhang, K., Van Gool, L., Timofte, R.: SwinIR: Image restoration using Swin Transformer. In: Proceedings of the IEEE/CVF International Conference on Computer Vision Workshops, pp. 1833–1844. (2021)
10. Gu, J., Lu, H., Zuo, W., Dong, C.: Blind super-resolution with iterative kernel correction. In: Proceedings of the IEEE/CVF Conference on Computer Vision and Pattern Recognition, pp. 1604–1613. (2019)
11. Huang, Y., Li, S., Wang, L., Tan, T.: Unfolding the alternating optimization for blind super resolution. In: Advances in Neural Information Processing Systems, pp. 5632–5643. (2020)
12. Wang, X., Xie, L., Dong, C., Shan, Y.: Real-ESRGAN: Training real-world blind super-resolution with pure synthetic data. In: Proceedings of the IEEE/CVF International Conference on Computer Vision Workshops, pp. 1905–1914. (2021)
13. Saharia, C., Ho, J., Chan, W., Salimans, T., Fleet, D. J., Norouzi, M.: Image super-resolution via iterative refinement. *IEEE Transactions on Pattern Analysis and Machine Intelligence* **45**(4), 4713–4726 (2022)

14. Chi, J., Sun, Z., Zhao, T., Wang, H., Yu, X., Wu, C.: Low-dose CT image super-resolution network with dual-guidance feature distillation and dual-path content communication. In: Medical Image Computing and Computer Assisted Intervention, pp. 98–108. (2023)
15. Liu, T., Chen, Z., Li, Q., Wang, Y., Zhou, K., Xie, W., Fang, Y., Zheng, K., Zhao, Z., Liu, S., Yang, W.: MDA-SR: Multi-level domain adaptation super-resolution for wireless capsule endoscopy images. In: Medical Image Computing and Computer Assisted Intervention, pp. 518–527. (2023)
16. Chen, Z., Zhang, Y., Gu, J., Kong, L., Yang, X.: Recursive generalization transformer for image super-resolution. In: International Conference on Learning Representations, (2023)
17. Rombach, R., Blattmann, A., Lorenz, D., Esser, P., Ommer, B.: High-resolution image synthesis with latent diffusion models. In: Proceedings of the IEEE/CVF Conference on Computer Vision and Pattern Recognition, pp. 10684–10695. (2019)
18. Clark, K.W., Vendt, B.A., Smith, K.E., Freymann, J.B., Kirby, J.S., Koppel, P., Moore, S.M., Phillips, S.R., Maffitt, D.R., Pringle, M., Tarbox, L., Prior, F.W.: The cancer imaging archive (TCIA): Maintaining and operating a public information repository. *Journal of Digital Imaging* **26**(6), 1045–1057 (2013)
19. Kingma, D. P., Ba, J.: Adam: A method for stochastic optimization. arXiv preprint arXiv:1412.6980 (2014)
20. Zhou W., Alan C.B., Hamid R.S., Eero P.S.: Image quality assessment: From error visibility to structural similarity. *IEEE Transactions on Image Processing* **13**(4), 600–612 (2004)
21. Li, C., Wong, C., Zhang, S., Usuyama, N., Liu, H., Yang, J., Naumann, T., Poon, H., Gao, J.: LLaVA-Med: Training a large language-and-vision assistant for biomedicine in one day. In: Advances in Neural Information Processing Systems, pp. 28541–28564. (2023)
22. Huang, Y., Wang, Q., Omachi, S.: Rethinking degradation: Radiograph super-resolution via aid-srgan. In: International Workshop on Machine Learning in Medical Imaging, pp. 43–52. (2022)
23. Zhou, H., Huang, Y., Li, Y., Zhou, Y., Zheng, Y.: Blind super-resolution of 3D MRI via unsupervised domain transformation. *IEEE Journal of Biomedical and Health Informatics* **27**(3), 1409–1418 (2022)
24. Lin, T., Chen, Z., Yan, Z., Yu, W., Zheng, F.: Stable diffusion segmentation for biomedical images with single-step reverse process. In: Medical Image Computing and Computer Assisted Intervention, pp. 656–666. (2024)
25. Tian, J., Aggarwal, L., Colaco, A., Kira, Z., Gonzalez-Franco, M.: Diffuse attend and segment: Unsupervised zero-shot segmentation using Stable Diffusion. In: Proceedings of the IEEE/CVF Conference on Computer Vision and Pattern Recognition, pp. 3554–3563. (2024)
26. Cho, J., Aghajanzadeh, S., Zhu, Z., Forsyth, D. A.: Zero-shot low light image enhancement with diffusion prior. arXiv preprint arXiv:2412.13401 (2024)
27. Jiang, H., Luo, A., Fan, H., Han, S., Liu, S.: Low-light image enhancement with wavelet-based diffusion models. *ACM Transactions on Graphics*, **42**(6), 1–14 (2023)
28. Radford, A., Kim, J.W., Hallacy, C., Ramesh, A., Goh, G., Agarwal, S., Sastry, G., Askell, A., Mishkin, P., Clark, J., Krueger, G., Sutskever, I.: Learning transferable visual models from natural language supervision. In: International Conference on Machine Learning, pp. 8748–8763. (2021)
29. Zeng, D., Huang, J., Bian, Z., Niu, S., Zhang, H., Feng, Q., Liang, Z., Ma, J.: A simple low-dose X-ray CT simulation from high-dose scan. *IEEE Transactions on Nuclear Science* **62**(5), 2226–2233 (2015)

30. Alexander Q.N., Prafulla D.: Improved denoising diffusion probabilistic models. In: International Conference on Machine Learning, pp. 8162–8171. (2021)
31. Ji, X., Cao, Y., Tai, Y., Wang, C., Li, J., Huang, F.: Real-world super-resolution via kernel estimation and noise injection. In: Proceedings of the IEEE/CVF Conference on Computer Vision and Pattern Recognition Workshops, pp. 466–467 (2020)